# Spatial Variations in Vent Chemistry at the Lucky Strike Hydrothermal Field, Mid-Atlantic Ridge (37°N): Updates for Subseafloor Flow Geometry From the Newly Discovered Capelinhos Vent

V. Chavagnac, T. Leleu, F. Fontaine, M. Cannat, G. Ceuleneer, A. Castillo

# Spatial Variations in Vent Chemistry at the Lucky Strike Hydrothermal Field, Mid Atlantic Ridge (37°N): Updates for Subseafloor Flow Geometry from the Newly Discovered Capelinhos Vent.

**V. Chavagnac[1], T. Leleu[1], F. Fontaine[2,3], M. Cannat[2], G. Ceuleneer[1], A. Castillo[1]**

[1] Geosciences Environnement Toulouse, Université de Toulouse, CNRS, IRD, UPS, Toulouse, France

[2] Institut de Physique du Globe de Paris, UMR CNRS 7154, Paris, France

[3] Observatoire Volcanologique du Piton de la Fournaise, La Plaine des Cafres, Réunion, France

Corresponding author : Valérie Chavagnac (valerie.chavagnac@get.omp.eu)

**Key points:**

- New hydrothermal vent named Capelinhos found at Lucky Strike hydrothermal vent
- New model of hydrothermal fluid circulation at Lucky Strike hydrothermal field
- Up to 65% of dissolved hydrothermal Fe stored along the hydrothermal up flow zone

## Abstract

This study aims at characterizing the subseafloor architecture of the Lucky Strike hydrothermal field (LSHF) based on an extensive chemical database of the various vents. Our analysis is motivated by the discovery in 2013 of a new active high-temperature site, named Capelinhos, approximately 1.5 km east of the LSHF. Capelinhos fluids display particular chemical features with chloride and metals (Fe, Mn) concentrations two times lower and four times higher, respectively, compared to other vent sites. Trace element partitioning over the entire chlorinity range indicates a single deep fluid source feeding all the venting sites. Applying the Si-Cl geothermobarometer at Capelinhos, we find phase separation conditions at 435–440°C, and 370-390 bars (2500–2800 m below seafloor (mbsf)) consistent with former estimates for the LSHF, while temperatures of fluid-rock last equilibrium are estimated at ~400°C for Capelinhos and 350-375°C for the other sites based on the Fe-Mn geothermometer. We interpret these discrepancies in thermodynamic conditions beneath the sites in terms of crustal residence time which are likely related to permeability variations across the hydrothermal upflow zone. We propose that conductive cooling of the up flowing fluids from the phase separation zone to the seafloor, beneath the main field vent sites, lowers the T conditions of last fluid-rock equilibrium, enabling ~65% of Fe mobilized in the reaction zone to be stored. In comparison, Capelinhos fluids are transported more rapidly from the reaction zone to the seafloor along a high-angle fracture system. The fluids venting at Capelinhos are more representative of the deeper part of the hydrothermal reaction zone.

## 1 Introduction

Hydrothermal fluid circulation at mid-ocean ridges (MOR) is one of the major processes controlling the cooling of the oceanic lithosphere (Chen & Morgan, 1990; Stein & Stein, 1994), the geochemical composition of the crust (Kelley & Delaney, 1987; Kelley & Robinson, 1990; Alt, 1995; Alt & Teagle, 2003; Barker et al., 2008; Brant et al., 2012), the chemical composition of the ocean (Elderfield & Schultz, 1996; Resing et al., 2015) and the development of peculiar chemo-synthetic ecosystems (Martin et al., 2008 and references therein). Increasing attention has been drawn to the study of black smokers since their discovery along the East Pacific Rise (EPR) off the Galapagos Islands in 1977. They have shown an unexpected diversity in geological setting, hydrothermal ecosystems and fluid chemistry (Campbell et al., 1988; Von Damm, 1988, 2000; Douville et al., 2002; Ludwig et al., 2006; Schmidt et al., 2007, 2011). From the recharge zone to the discharge area, seawater is transformed into a high temperature hydrothermal fluid, acquiring its chemical composition in a reaction zone, which is univocally pictured on top of axial magmatic chambers (AMC) at least along magmatically robust sections of fast (e.g. EPR, 9º50'N), intermediate (e.g. Endeavour segment, Juan de Fuca Ridge) and slow spreading (e.g. Lucky Strike, 37º17'N) ridges. The chemical composition of high temperature fluids can be further modified by either interaction with the rocks along the upflow pathway to the seafloor or precipitation of secondary minerals, depending on the fluid velocity (Saccocia & Seyfried, 1994; Lowell, 2003; Coogan, 2008; Steele-MacInnis et al., 2012). Thus highlights that the P-T estimates for reaction zone conditions are sensitive to the geochemical tracer used and clear depth boundaries of the reaction zone cannot be easily drawn. The water-rock interactions which form hydrothermal fluid formation from seawater, occur over a wide range of pressure and temperature conditions, i.e. from the deepest part of the hydrothermal cell to the discharge at the seafloor, $\Delta P$ and $\Delta T$ can be a few hundred bars and °C, respectively. Chemical variations can be identified depending on the nature of the substratum, i.e. extrusive

basaltic and/or mantellic substrate. The chemical compositions of focused hydrothermal fluids are used to constrain the range of pressure and temperature conditions at which water-rock interactions take place in the crust (Seyfried et al., 1998; Seyfried, 2003; Von Damm et al., 2003; Mottl et al., 2011; Reeves et al., 2011). The purpose of the present study is to gain insight on the subseafloor flow geometry using chemical analysis on fluids from different sites at the Lucky Strike hydrothermal field (LSHF).

LSHF was discovered at 37ºN along the slow-spreading Mid-Altantic Ridge (MAR) in 1992 during the FAZAR cruise (Langmuir et al., 1997). The discovery motivated several subsequent research cruises with the objective of better characterizing the geological, geochemical, geophysical and biological context of the vents (Fouquet et al., 1995; Langmuir et al., 1997; Von Damm et al., 1998; Charlou et al., 2000; Ondréas et al., 2009; Barreyre et al., 2012; Pester et al., 2012; Escartin et al., 2015). The first comprehensive study on the LSHF vent chemistry (Von Damm et al., 1998) indicated that the discharge of focused fluids (sampled in 1993 and 1996) originated from deep rooted fluids that underwent near-surface processes, e.g. mixing with seawater, in the upflow zone (Von Damm et al., 1998). Charlou et al. (2000) analyzed fluids from ten active sites of the LSHF. All samples were depleted in chloride relative to seawater (~420mM to ~520mM) with Cl increasing along a SE-NW transect across the LHSF. These authors proposed that a relatively shallow reaction zone provided vapor-like fluids (i.e., Cl below 545 mM of seawater) to the upflow zone at subcritical conditions (temperature and pressure lower than 407°C and 298bars respectively, equivalent to ~1300 mbsf; Bischoff, 1991). Chemical data presented by Charlou et al. (2000) also suggested that vapor-dominated fluids underwent substantial subsurface mixing with altered seawater prior to venting as indicated by variable Sr isotope signatures with Cl concentrations still below that of seawater.

Eleven years later, Pester et al. (2012) used trace element and chloride co-variation in fluids at five active vents to infer P–T equilibrium conditions during upflow. The samples display both

chloride depletion and enrichment relative to seawater (from 414mM to 588mM). These authors proposed that 1) a unique and deep source feeds the hydrothermal field and 2) fluids underwent phase separation at 430–475°C and 410–480 bars (~2400–3100 mbsf), i.e. much higher P-T conditions than those proposed by Charlou et al. (2000). They attributed the variability observed in fluid chlorinity to subtle changes in pressure and/or temperature. These authors also argue that after phase separation and prior to discharge, the hot fluids cooled conductively and equilibrated with the greenschist facies of basaltic host rocks at lower temperatures (i.e. 350–380 °C).

These different models of the plumbing circulation system below the LSHF highlight the difficulties that arise when interpreting the chemical composition of vent fluids. This is compounded by the lack of contemporaneous observations between the studied sites. The EMSO-Azores program started in 2010 (FP6-ESONET; Person et al., 2009; Colaço et al., 2011) and led to the set-up of a deep-sea observatory at LSHF. High temperature hydrothermal fluids were collected yearly during maintenance cruises which permitted the discovery of a new, high-temperature venting site, named Capelinhos (T=324°C, Table 1) in 2013 (Escartin et al., 2015; Fig 1). Capelinhos lies approximately 1.5 km east of the LSHF and a few hundred meters from the seafloor emergence one of the normal faults (referred as F2 in Combier et al., 2015) that rifts the Lucky Strike axial volcano. All other active/inactive venting sites are located to the west around a fossil lava lake on top of the volcano (Humphris et al., 2002; Ondréas et al., 2009; Barreyre et al., 2012; Fig 1).

In this study, we report on the first chemical data acquired for the Capelinhos vent site and we compare its chemical characteristics with those from 12 other active LSHF vents sampled during the same cruise in 2013. We use this dataset to show that Capelinhos is a key site to assess the role of subsurface mixing, phase separation, and conductive cooling processes on the

chemistry of the LSHF fluids and to propose an up-dated model of hydrothermal circulation below the field.

## 2 Geological setting

The ~65 km long Lucky Strike segment is located south of the Azores islands along the MAR between 37°03'N and 37°37'N (Detrick et al., 1995). The spreading rate is ~22 mm/yr (Cannat et al., 1999; Miranda et al., 2005). The LSHF is located on top of a volcano at the center of the segment. Seismic data have constrained the presence of an axial magma chamber (AMC) at a depth of about 3500 m below the summit of the volcano (Singh et al., 2006). Microseismic events recorded between 2007 to 2009 are located above the AMC at depths between 1800 and 2500 m below seafloor (mbsf), and interpreted as the product of active fracturing induced by penetration of colder down-flowing fluids into the hot rocks (Crawford et al., 2013). These microseismic events document the existence of two predominantly along-axis hydrothermal cells, with a central upflow zone centered beneath the LSHF. Seismic data suggests that the layer 2A depth is variable throughout the hydrothermal field (Arnulf et al., 2011).

The long known Lucky Strike hydrothermal field (Von Damm et al., 1998, Charlou et al., 2000, Pester et al., 2012; Chavagnac et al., 2018 Fig.1) comprises 20-30 sites with high-temperature black smokers (T= 200-340°C) and low-temperature diffuse venting (total area about 1800 $m^2$, Barreyre et al., 2012). These sites are all clustered around a fossil lava lake (300 m in diameter; Fouquet et al., 1995) framed by two ancient volcanic cones, and one of which has been truncated by N010°–N030° faults and fissures (Ondréas et al., 2009; Fig 1). The newly discovered Capelinhos site is isolated and located 1.5 km to the east of the main field (Escartin et al., 2015). There, chimneys form “candelabra-like structure” on top of 10 m high sulfide mound and expel black smoker-type fluids at temperatures up to 324°C (Figure 2; Table 1). Diffuse venting is limited to the close vicinity of the black smokers, at the base of the edifice.

## 3 Sampling and Analytical Methods

### 3.1 Fluid collection

The fluid samples studied in this paper were collected during the MoMARsat'13 EMSO-Azores maintenance cruise on the French Research vessel *Pourquoi Pas?* in September 2013. The 13 sampling sites (12 on LSHF and Capelinhos) were chosen to document the fluid diversity identified at LSHF by previous studies (Von Damm et al., 1998; Charlou et al., 2000; Pester et al., 2012; Chavagnac et al., 2015). Each vent site was sampled four times in succession (total duration of sampling <1 hour) to allow a better characterization of the end-member hydrothermal fluid. In-situ temperatures were measured in each vent prior to fluid sampling using the ROV Victor 6000 high temperature probe. High-temperature fluids were collected with 200ml titanium gas-tight samplers handled and triggered by the hydraulic arm of the ROV. The time between fluid samples at a given vent did not exceed 20 minutes. The samples were processed on board immediately after the ROV recovery. First, gases were extracted from the samplers and transferred into vacuumed stainless steel canisters or to ultra-clean water sealed glass bottles, depending on the expected gas volume, for further analysis. The fluid samples were then extracted, filtered through 0.45 µm Millipore filters and split into different aliquots for onshore analysis and stored at 4°C. pH, Eh, salinity and conductivity were measured on-board immediately after gas/fluid processing.

### 3.2 Analytical methods

All the chemical analyses were conducted at the Geosciences Environment Toulouse (GET) laboratory. Ca, Na, K, Mg, Si, Fe, Mn and Li concentrations were determined with an inductively coupled plasma atomic emission spectrometer (ICP-AES) Horiba Ultima2 instrument. Errors on analyses are indicated in Table 2. The instrument is calibrated using mono elemental solutions, multi elemental solutions, and IAPSO standard solution (Besson et al.,

157 2014). The latter is a seawater standard solution provided by OSIL and certified for its salinity.
158 Salinity controls major element concentrations in seawater (Millero et al., 2008). Li
159 concentration measurements of IAPSO give an average concentration of 24.6 ± 0.3 µM
160 (rsd=1%; n=4; 26.5 µM for seawater, Von Damm et al., 1998). The analytical drift is quantified
161 by the standard bracketing after every 8 samples. Analytical precision is better than 2%.

162 Sr, Rb and Cs concentrations were measured using an inductively coupled plasma mass
163 spectrometer ICP-MS Agilent500. The standard used was a NASS 6 solution (international
164 seawater standard certified for some trace metals) and give values of 79.1 µM, 1.17 µM, 1.19
165 nM compared to 87 µM, 1.4 µM and 2 nM of seawater values for Sr, Rb and Cs respectively
166 (n=3). Drift corrections are made using an in-house multi-elementary standard doped with In
167 and Re before analysis. Anions (Cl, $SO_4$, Br) were determined by anionic chromatography
168 calibrated with a IAPSO standard seawater solution.

169 Sr isotopic composition was measured at the GET laboratory using a MAT FINIGAN 261
170 thermal ionization mass spectrometer. Analyses were performed on the samples which contain
171 the lowest Mg concentrations. Sr was isolated from the matrix using Sr-Spec resin (Eichrom,
172 USA). The $^{87}Sr/^{86}Sr$ ratio was defined as the average of 100 measurements of ion intensities
173 following the static multi-collection mode. The $^{87}Sr/^{86}Sr$ ratios were normalized to $^{86}Sr/^{88}Sr$ =
174 0.1194. Measured values for NBS 987 standard (recommended values of 0.710250) was
175 $^{87}Sr/^{86}Sr = 0.710250 \pm 0.000011$ ($2\sigma_D$, n = 14).

176 We consider end-member hydrothermal fluids calculated by linear extrapolation to zero-Mg of
177 the least-square regression method (Table 2; Von Damm, 1988). The compositions of all
178 analyzed samples for Sr isotope signature are given in the Supplementary Materials (Fig S1 and
179 Table S1). For isotopic composition, the same method of linear extrapolation to a Mg/Sr equal
180 to zero is used.

## 4. Results

*Chloride, Sulfate, Bromide*

Hydrothermal fluids of the LSHF exhibit chloride concentrations between 415 mM for the South-East (SE) sites (Montsegur, Aisics, and Tour Eiffel; Figure 1) and 574 mM for the North-East (NE) sites (Y3 and Sintra) and the South-West (SW) sites (South Crystal, Crystal and Sapins). White Castle, Isabel and Cyprès sites have Cl concentration closer to seawater one at values ranging between 470mM and 520mM, also in line with previous data. Interestingly, Capelinhos has the lowest chloride concentration ever measured at LSHF at 262 mM (Table 2).

All fluids have $SO_4$ values close to zero. However, some of them (Crystal and Tour Eiffel) have calculated end-member value slightly higher than 0 probably due to anhydrite entrainment and dissolution (Von Damm et al., 1998; Table 2). Br concentrations have variations similar to Cl concentrations, whereby maximum Br concentrations are found in Y3 fluids at 0.88 mM close to the seawater value of 0.84 mM while minimum values are found for Capelinhos fluids at 0.38 mM.

*Iron and Manganese*

Capelinhos end-member fluid shows very high Fe and Mn concentrations of 2789 µM and 639 µM, respectively. In comparison, Fe and Mn concentrations of LSHF end-member fluids vary between 155 µM (Sintra) and 593 µM (South Crystal) for Fe (Fig 3a) and between 164 (Sintra) and 232 µM (South Crystal) for Mn (Fig 3b).

*Silica*

Silica concentrations of hydrothermal end-members vary from 12.8 mM at Sintra (NE group) to 18.6 mM at Cyprès (SW group). The Si concentration at Capelinhos is 14.1 mM, a value similar to the one for the SE sites, despite distinct chlorinities (Fig 3c).

*Sodium, Calcium and Potassium*

Na, Ca and K constitute the major cations in the end-member fluids and are closely linked to Cl concentration due to charge balance. Maximum Na concentrations (445mM) are found in Crystal and South Crystal fluids, while the minimum Na concentration (205 mM) is obtained for Capelinhos.

Maximum Ca concentration are found in Sintra, Y3, Crystal and South Crystal fluids with values around 53 mM while at Capelinhos the Ca concentration is the lowest one at 18mM.

Maximum K concentrations (28.3 mM) are found in South Crystal and Crystal and the minimum concentration (12.1 mM) is measured at Capelinhos.

*Rubidium, Strontium, Cesium and Lithium*

Rb, Cs and Li are ten to 20 times more enriched in the LSHF fluids compared to seawater while Sr concentrations fluctuate around the seawater value at ± 20%. Concentrations in Rb, Li, Cs and Sr are correlated to the fluid chlorinity (Table 2). Minimum and maximum Rb concentrations are 18.7 µM and 50 µM for Capelinhos and Crystal, respectively. Minimum and maximum Li concentrations are 197.1 µM and 367.9 µM, also for Capelinhos and Crystal, respectively. Sr follows the same pattern with a maximum concentration of 180 µM for Crystal and a minimum concentration of 35.9 µM at Capelinhos.

*Sr isotopes*

The least radiogenic end-member fluid compositions ($^{87}Sr/^{86}Sr$=0.70384; Table 2) are obtained for Capelinhos. Y3, Crystal and South Crystal on the Northern and Western side of the fossil

lava lake have unradiogenic $^{87}Sr/^{86}Sr$ ratios ranging between 0.7039 and 0.7040. $^{87}Sr/^{86}Sr$ signatures of the Aisics, Tour Eiffel, and Montsegur sites are the most radiogenic ones at 0.7042 - 0.7043 (Table 2). The Central sites display variable Sr isotope signatures, i.e. Cyprès at 0.70403 and White Castle at 0.70502.

## 5. Discussion

### 5. 1 Source(s) of hydrothermal fluids

Cl is the major anion present in hydrothermal fluids, and controls the cation abundances due to the charge balance of the solution. We propose to define groups of sites based on Cl concentrations and spatial distribution on the seafloor. With the lowest salinity, Capelinhos (Cl = 262mM) defines its own group; the SE group of sites is composed of Tour Eiffel, Montsegur, Aisics with a $Cl_{average}$ of ~420mM; the Central group characterized by $Cl_{average}$ ~495mM, comprises Isabel, White Castle, Cyprès. We define SW and NE groups for which salinity values are all close to or above seawater, i.e. SW group (Crystal, South Crystal, and Sapin sites; $Cl_{average}$: ~580mM) and NE group (Y3 and Sintra sites; $Cl_{average}$: 574 and 537 mM). Due to the conservative behavior of Cl in hydrothermal system, this chemical tracer has been widely used to infer the P-T conditions of the phase separation zone. Charlou et al. (2000) proposed that Cl variability observed at the LSHF could be due to subcritical vapors mixing with altered seawater in subsurface conditions prior to fluid venting. To address this hypothesis, we use the Sr isotope compositions of the lowest Mg-rich hydrothermal fluids as a tracer of sources and mixing.

A hydrothermal fluid acquires its Sr isotopic signature from the rocks with which it interacts (Albarède et al., 1981), i.e basalt at LSHF. The contrasting Sr isotope compositions of basalt at 0.70298 and seawater at 0.70916 are favorable to the detection of any input of modified seawater in hydrothermal fluids. Any Sr isotopic signature of hydrothermal fluid end-member that departs from that of the basalt, will suggest the contribution from an additional source

(Berndt et al., 1988; Palmer, 1992; Ravizza et al., 2001). The most vapor-dominated fluid at Capelinhos exhibits the least radiogenic Sr isotopic composition at 0.70384. In comparison, the SE, NE and SW groups which exhibit Cl concentrations at 420mM, 574mM and 570mM, respectively, display similar Sr isotopic signatures at 0.7042-0,7044 for SE sites and 0.7040 and 0.7042 for NE and SW sites (Table 2). In contrast, the Central group (˜495mM of Cl) displays a wide range of $^{87}Sr/^{86}Sr$ ratios, ranging from 0.70403 to 0.70502. The observed range of $^{87}Sr/^{86}Sr$ ratios of fluid end-members do not correspond to the geographical distribution of sites around the fossil lava lake. Moreover, the $^{87}Sr/^{86}Sr$ ratios and the Cl contents of hydrothermal end-members do not correlate positively and linearly. In addition, it is unlikely that the variability of $^{87}Sr/^{86}Sr$ ratios is related to local differences in the substratum, as basalts from a wide selection of samples (including T- and E-MORB) across the Lucky Strike segment have a well-constrained Sr isotopic signature of 0.70298±0.00007 (n=13; Hamelin et al., 2013). The tight but significant differences in Sr isotopic signature between the highest and lowest chlorinity fluids means that Capelinhos fluid, compared to the other sites, has less interaction with radiogenic Sr-rich material such as extensively altered rocks. The fact that $^{87}Sr/^{86}Sr$ is not correlated with Cl rules out a modified seawater component that would mix with hydrothermal fluid in subsurface. However, this does not rule out the contribution of a second deep-rooted hydrothermal cell to produce the Capelinhos fluid.

We investigate the distribution of trace element concentrations (Br, Li, Sr, Rb and Cs) over the LSHF chlorinity range, following the methodology of Pester et al. (2012) to detect the potential occurrence of a second hydrothermal source. The elements considered are controlled by vapor/brine partition coefficients during phase separation (Pester et al., 2015; Foustoukos & Seyfried, 2007a, b; Foustoukos et al., 2004; Berndt & Seyfried, 1990; among others). Li and Cs distributions exhibit a negative linear trend while Rb and Sr show a positive trend, indicating a preferential partitioning to the vapor and brine phases, respectively (Figure 4). This is in line

with previous studies (Berndt & Seyfried, 1990; Pokrovski et al., 2005; Foustoukos & Seyfried, 2007a; Pester et al., 2015). This is also coherent with the LSHF study of Pester et al. (2012), apart for Rb which shows less brine affinity with the extended Cl range of the present dataset. Note, however, that without Capelinhos fluid, Rb presents a steeper linear slope at +0.38, identical to the one at +0.35 reported in Pester et al. (2012). Element vapor/brine partitioning can be summarized as follow Sr<Rb<<Br<<Cs<Li with increasing affinities for the vapor phase. Therefore, the linear correlation of each of these elements over the Cl range (from 262mM to 574mM; Figure 4) supports a phase separation process controlling overall trace element abundances, i.e. a unique deep-rooted fluid source as proposed by Pester et al. (2012). This implies that being 1.5 km away from the other sites, Capelinhos is nevertheless fed by the same upflow zone and is part of the same hydrothermal cell.

### 5. 2 Chlorinity variability and geographical repartition

While the distribution of trace element suggests a unique source feeding the hydrothermal upflow at LSHF, the end-member fluids nevertheless display a wide range of chlorinity, from the most vapor-like, low-Cl fluids at Capelinhos to the brine-like, high-Cl fluids at Y3. Venting of low-Cl fluids can unambiguously be ascribed to phase separation processes at depth and flushing of buoyant vapor phase on the seafloor. However, the physics controlling the venting of brine-like fluids is more complex as their thermodynamical (viscosity and density) and surface properties (surface tension) counteracts their buoyancy, impacting therefore their rise towards seafloor. In the literature, numerical models of two-phase flow including transport of salt (considered as NaCl) have proposed scenarios for brine venting (Fontaine et al., 2007; Coumou et al., 2009).

Phase separation leads to vapor and brine formation but due to different physical behavior, i.e. the wetting effect of the liquid/brine phase, brines will segregate and be stored in backwater

298 porosity or will coat the walls of larger channels (Fontaine & Wilcock, 2006). As long as brine
299 saturation is lower than a threshold value, the brines do not form a continuous medium and
300 remain immobile. However, when this threshold is reached, and provided that the vertical
301 pressure gradients in the upflow are high enough compared to brine density (if not, the brine is
302 too dense and will sink down; Fontaine & Wilcock, 2006; Fontaine et al., 2007), then the brine
303 phase is able to move upwards. Fontaine and Wilcock (2006) showed that brine (<20-25wt%
304 NaCl) produced under supercritical conditions and stored within the rock backwater porosity
305 in the reaction zone, could still flow towards the surface. Meanwhile, vapor phases flow
306 preferentially through wider cracks (Goldfarb & Delaney, 1988; Fontaine & Wilcock, 2006)
307 and are flushed to the seafloor. Fontaine et al. (2007) also developed the hypothesis that vertical
308 permeability gradients could act as a barrier for brine upflow and tend to concentrate brine at
309 the base of layer 2A. When the backwater porosity is saturated with brine, or during cooling of
310 the system, brine can be entrained, and mixed with vapor or seawater salinity hydrothermal
311 fluid, which leads to fluid discharge with higher salinity than seawater.

312 Alternatively, Coumou et al. (2009) conducted numerical modelling without a permeability
313 gradient to investigate salinity variations at discharge zones for different bottom heat fluxes and
314 system pressures. For a pressure of 150 bars at the seafloor and ~250 bars at the bottom of the
315 system, i.e. phase separation zone ~1000mbsf, the simulations show temporal variations in vent
316 fluid salinity with several spikes at salinity higher than seawater over periods of several years.
317 These salinity spikes are also associated with temperature spikes of a few degrees (<10°C).
318 Coumou et al. (2009) explained these salinity pulses as due to brine mobilization occurring
319 when the porosity of the upflow zone becomes saturated. Further mixing of this brine with
320 vapor-dominated fluids during the upflow produces a transient spike in salinity. Salinity then
321 returns to the initial vapor-like one, while the brine layer builds up again and reduce saturation
322 of the backwater porosity. In summary, modeling studies infer that sustained phase separation

processes can drive brines to “over-saturate” the porous network causing their remobilization and flushing to the seafloor without major changes in the thermodynamic state of the hydrothermal cell.

Brine remobilization and flushing have been already observed and invoked in the natural hydrothermal environment, to explain Cl variability related to periodic (tides) brine flushing at the Main Endeavour Field (Larson et al., 2009). At LSHF, Y3 site exhibits Cl concentrations which increase from vapor-like values at 436 mM in 1993 (Von Damm et al. 1998) to brine-like ones at 574 mM in 2013 (this study, Table 2). We infer that this shift in fluid chlorinity of Y3 site could be ascribed to brine over-saturation and mobilization in the porous/fractured crust along the upflow zone, as venting temperature and reaction zone P-T conditions according to the geothermobarometers did not fluctuate significantly over that time period (Pester et al. 2011). Based on a study of tidal forcing on LSHF vent fluid temperatures, Barreyre and Sohn (2016) proposed that the permeability structure beneath the LSHF vents is variable, possibly reflecting variations of layer 2A thickness from 300 to 600 mbsf between the west and east of the fossil lava lake area. Such local variations would also be expected to impact brine storage and remobilization beneath the field. Finally, the yearly monitoring of the Y3 vent in comparison to other LSHF sites should provide key information of the temporal evolution of brine venting. Such information is particularly important to better design numerical models of hydrothermal flow dynamics and to gain more insight into the interrelationships between phase separation, brine storage, remobilization and fate beneath the field.

### 5.3 Pressure and Temperature Conditions in the LSHF hydrothermal system

#### 5.3.1 Conditions at the base of up-flow zone

Si and Cl end-member fluid concentrations have been used as a geothermobarometer to determine the depth of the top of the two-phase zone in several hydrothermal systems

worldwide (Fontaine et al., 2009). This depth is considered a good estimate of the base of the upflow zone as phase separation induces large variations in the fluid fluxibility (a measure of the ability of buoyancy-driven water to transport energy), providing the necessary buoyancy for the hydrothermal vapors to flow upwards (Jupp & Schultz, 2000; Coumou et al., 2009). Cl concentration only changes in the two-phase zone, as soon as the vapor-dominated fluid starts to rise it returns to a single-phase, and its Cl content is fixed for the remainder of the ascent to the seafloor, provided no mixing with seawater occurs. The Cl content of flushed vapors are thus representative of the conditions at the top of the two-phase zone. Using Cl-P-T solubility relationships (e.g., Driesner, 2007), one can estimate a range of possible conditions (a iso-Cl line) in P-T space for a given Cl. Now, considering that Si is in equilibrium with quartz during upflow/cooling and using Si-Cl-T-P solubility relationships (e.g., Foustoukos & Seyfried, 2007b) one can use the Cl and Si contents of the vented vapors to estimate another range (an iso-Si line) of possible T-P for a given Si. Intersection between these iso-Cl and iso-Si lines gives a unique P-T condition for the roof of the two-phase area. When applying the Si-Cl geothermobarometer to the Capelinhos fluids, we obtain a temperature of 438°C and a pressure of 375 bars for the phase separation zone/base of the reaction zone, that corresponds to a depth of 2600 mbsf (using a cold hydrostatic pressure gradient of $\rho$=800kg/m$^3$, Fontaine et al., 2009). Using the Tour Eiffel chemical data for fluids collected in 1993 (Charlou et al., 2000), Fontaine et al. (2009) determined similar P and T conditions at 390 bars and 440°C for the LSHF phase separation zone. Thus, the deepest part of the upflow zone is quite well constrained with similar estimates for fluids collected 20 years apart and at different site within the LSHF.

One should, however, be careful using this geothermobarometer as quartz may precipitate during upflow. Quartz veins in the ocean crust are often associated to greenschist facies minerals such as pyrite, chlorite, amphibole and epidosite at different depth levels (Delaney et al., 1987; Honnorez, 2003; Heft et al., 2008; Alt et al., 2010). The vented Si concentration

should, therefore, be taken as a minimum value (the actual Si content of the rising vapor being higher and not constrained) giving a minimum depth to the base of the upflow/roof of the two-phase area. The Si-Cl geothermobarometer developed by Fontaine et al. (2009) predicts that the estimated depth of the top of the two-phase zone would deepen by 70-100m per mmol of Si at constant Cl. We note that the equilibrium pressure ranges of 375-390 bars derived with Si-Cl, i.e. 2600-2800 msbf is in good agreement with the 2300-2900 mbsf maximum depth range for micro-seismic activity beneath the hydrothermal field (Crawford et al., 2013).

### 5.3.2 Conditions of last equilibrium in the reaction zone

Vent fluid Fe and Mn contents can be used to estimate the temperature of the fluid last equilibrium with greenschist facies rocks (Pester et al., 2011). For Capelinhos end-member fluids, which exhibit the highest Fe and Mn concentrations of all the LSHF fluids - equivalent to Fe concentration found at the Broken Spur (29°N) and Snake Pit (23°N) fields on the MAR (Campbell et al., 1988; James et al., 1995; Figure 5) - we find a minimum temperature of greenschist facies equilibrium at 403°C. The Fe-Mn geothermometer does not provide a means to calculate a corresponding equilibrium pressure. If we assume that both quartz and fluid-greenschist (Fe and Mn bearing) minerals facies reached equilibrium concomitantly, i.e. that the Capelinhos fluids interacted minimally with the surrounding rocks during their ascent from the phase separation zone, then the equilibrium temperature is obtained from the Fe-Mn geothermometer and the vent fluid Si concentration permits to calculate a corresponding equilibrium pressure using Cl-T-P-dependent solubility relationships (Von Damm et al., 1991; Foustoukos & Seyfried, 2007b). At Capelinhos (Si=14.1 mM, Cl=260 mM), the estimated equilibrium pressure is 350 bars, i.e. a depth of ~2300 mbsf (Fig 5a). Applying the same approach to the most brine-dominated hydrothermal fluids from the other LSHF sites, i.e. the SW group and Y3 of the NE group, indicates a lower pressure (300 bars, i.e. ~1600 mbsf) and cooler temperatures 350-375ºC for the last fluid-rock equilibrium. These differences in P-T

conditions of last fluid-rock equilibrium between the Capelinhos and the other LSHF sites probably indicates that the fluids venting at Capelinhos ascend more rapidly from the phase separation zone than the fluids venting at the other sites so that they react less with the lost rocks upon ascent. This interpretation is also consistent with the least radiogenic Sr isotope signature of Capelinhos end-member fluids which we interpret as the most representative of the basaltic substratum (section 5.1). We thus propose that the observed variability in fluid composition between the LSHF vent sites primarily results from variable fluid residence times within the different areas that compose the upflow zone. We discuss a possible geological factor controlling these processes at Lucky Strike in the next section.

### 5.4 Fluid circulation pathway at LSHF

Based on the Si-Cl geothermobarometer which is in agreement with the depth of micro-seismic activity (Crawford et al. 2013), we propose that fluids at Lucky Strike start to upflow from a depth/pressure of 2600-2800 mbsf/370-390 bars at 430-440 °C below the lava lake. Capelinhos is located 300 m to the east of a west-dipping fault that has been imaged in seismic reflection data and shown to extend at least down to a few hundred mbsf under the volcano (F2 in Combier et al., 2015; Figure 6). We infer that small offset faults and fractures parallel to this fault and belonging to the same network may intersect the seafloor near Capelinhos (Escartin et al., 2015). We propose that this fault and fracture network intercepts the hydrothermal upflow zone at depth, in the intrusive section (layer 2B), creating a fast-extraction pathway for hydrothermal fluids venting at Capelinhos because of enhanced hydraulic properties (e.g., permeability, porosity) due to tectonically produced faults and fissures (Caine et al., 2010) (Figure 6). This "transverse" and longer (compared to a vertical flow) flow path leads to significant cooling from 403°C in the phase separation zone to 324°C at the vent field but the fast fluid migration and short residence time prevents extensive fluid-rock reactions, and the exiting fluids preserve their metal content. On the other hand, the fluids exiting at the main LSHF sites distributed

around the lava lake would rise almost vertically, but more slowly due to the lower overall permeability of younger intrusives beneath the fossil lava lake (Arnulf et al., 2011). This longer residence time allows fluids to interact more extensively with the crust to temperature down to 350°C, and to precipitate a large part of their metal content, as secondary greenschist minerals including Fe-bearing phases like chlorite.

The low Fe-Mn ratios of the main LSHF sites (˜0.8 to 2.5), compared to Capelinhos fluids at ˜4.4 (Fig 4), reflects a significant Fe loss within the upflow zone. By using Capelinhos fluids as a reference, we calculate that ˜65% (±14%) of dissolved hydrothermal Fe from sites located around the fossil lava lake is stored most likely as secondary minerals between the phase separation zone and the seafloor. In other words, only ~35% of Fe mobilized in the reaction zone is discharged as dissolved phase into the deep seawater mass at the LSHF.

## 6 Conclusion

In 2013, a new active site, named Capelinhos, was discovered at LSHF approximately 1.5 km east of the main Lucky Strike axial graben and fossil lava lake, where the well-known LSHF vents are located. Capelinhos vents high temperature black smoker fluids at 324°C. Its fluid chemistry has two distinct characteristics compared to the other LSHF vent sites: 1) the lowest Cl concentration at ˜260 mM ever measured at LSHF and 2) the highest Fe and Mn concentration (2800 μM and 640 μM respectively). The discovery of this site provides the opportunity to reassess the thermodynamic condition within the reaction zone. Applying the Si-Cl geothermobarometer of Fontaine et al. (2009), we show that Capelinhos fluids were formed at supercritical conditions, as well as the other vapor-dominated fluids from LSHF. The temperature of the phase separation zone is 438°C at 2600mbsf. These results are in agreement with the maximum depth of microseismic events reported in Crawford et al. (2013) which are

interpreted as due to rapid heat exchange between hot rocks and down-going hydrothermal fluids.

Applying other geochemical indicator, such as Fe–Mn geothermometer of Pester et al (2011), a range between ~370°C for LSHF fluids and ~400°C for Capelinhos is obtained. By combining quartz solubility with these calculated temperatures, the minimum equilibration temperature and pressure in the reaction zone appears to be deeper for Capelinhos fluids (350 bars) than for LSHF (300 bars). Because the fluids vent at temperatures that are still well within the greenschist facies realm, these conditions are not considered as completely representative of the top of the reaction zone. More accurately, they are indicative of significant differences in the residence time of the fluid in the upflow zone between Capelinhos and the other LSHF vents.

We propose a revised model of the hydrothermal path based on the discovery of Capelinhos. When crossing the 2-phase boundary, at ~2600 mbsf, the fluid starts flowing upwards, with brine entrainment to different extent from site to site. At the fossil lava lake, fluids (vapor and brines) undergo more conductive cooling than Capelinhos vent along their upflow to the surface due to longer residence time in the substratum. Brine mixing and cooling processes likely result in the formation of secondary Fe-bearing minerals like chlorite beneath the fossil lava lake, resulting in the storing of up to 65% of Fe mobilized in the reaction zone. Fluids discharging at Capelinhos (the most vapor dominated fluid of the LSHF), reach the sea-surface by a high angle normal fault zone, and undergo significant cooling but still preserve high dissolved Fe and Mn concentrations.

**Acknowledgements**

We thank the *Pourquoi Pas?* and Genavir crew as well as the ROV team for their tremendous work during the cruise. We are grateful to the chemistry facility of the Géoscience Environment

Toulouse laboratory (GET). Supplementary materials provide geochemical and Sr isotope signature of hydrothermal fluids. All geochemical measurements made aboard are available in the cruise report at the following doi: http://dx.doi.org/10.17600/13030040. Leleu acknowledges the French Ministry of Education and Research for the financial support of his Ph.D. fellowship. We also acknowledge financial support from the French ANR Lucky scales project (ANR-14-CE02-0008-03) and the EU project EMSO (http://www.emso-eu.org/). We are also grateful for the suggestions and constructive comments of N. Pester, W. Wilcock, J.A. Resing and two anonymous reviewers on different versions of this manuscript.

478 **References**


479 Albarède, F., Michard, A., Minster, J.-F., & Michard, G. (1981). $^{87}Sr/^{86}Sr$ ratios in hydrothermal
480 waters and deposits from the East Pacific Rise at 21°N. *Earth Planetary Science Letters,* 55,
481 229–236.

482 Alt, J. C. (1995). Seafloor processes in mid-ocean ridge hydrothermal systems. in *Seafloor*
483 *Hydrothermal Systems: Physical, Chemical, Biological, and Geological Interactions* edited by
484 S. E. Humphris, R. A. Zierenberg, L. S. Mullineaux, & R. E. Thomson (Ed), pp. 85-114, AGU
485 monograph 91, Washington, D. C.

486 Alt, J. C., & Teagle, D. A. H. (2003). Hydrothermal alteration of upper oceanic crust formed at
487 a fast-spreading ridge: mineral, chemical, and isotopic evidence from ODP Site 801. *Chemical*
488 *Geology,* 201, 191–211, doi:10.1016/S0009-2541(03)00201-8.

489 Alt, J. C., Laverne, C., Coggon, R. M., Teagle, D. A. H., Banerjee, N. R., Morgan, S., et al.
490 (2010). Subsurface structure of a submarine hydrothermal system in ocean crust formed at the
491 East Pacific Rise, ODP/IODP Site 1256. *Geochemistry, Geophysics, Geosystems,* 10, 1-28. doi:
492 10.10292010GC003144.

493 Arnulf, A. F., Singh, S. C., Harding, A. J., Kent, G. M., & Crawford, W. (2011). Strong seismic
494 heterogeneity in layer 2A near hydrothermal vents at the Mid-Atlantic Ridge. *Geophysical.*
495 *Research Letters,* 38, doi:10.1029/2011GL047753.

496 Barker, A. K., Coogan, L. A., Gillis, K. M., & Weis, D. (2008). Strontium isotope constraints
497 on fluid flow in the sheeted dike complex of fast spreading crust: Pervasive fluid flow at Pito
498 Deep. *Geochemistry, Geophysics, Geosystems,* 9, doi:10.1029/2007GC001901.

499 Barreyre, T., Escartín, J., Garcia, R., Cannat, M., Mittelstaedt, E., & Prados, R. (2012).
500 Structure, temporal evolution, and heat flux estimates from the Lucky Strike deep-sea

hydrothermal field derived from seafloor image mosaics: Hydrothermal outflow and image mosaics. *Geochemistry, Geophysics, Geosystems,* 13, doi:10.1029/2011GC003990.

Barreyre, T., & Sohn, R. A. (2016). Poroelastic response of mid-ocean ridge hydrothermal systems to ocean tidal loading: Implications for shallow permeability structure: Shallow Upflow Zone Permeability. *Geophysical Research Letters,* 43, 1660–1668, doi:10.1002/2015GL066479.

Berndt, M. E., Seyfried Jr, W. E., & Beck, W. J. (1988). Hydrothermal alteration processes at Mid-Ocean Ridges: Experimental and theoretical constraints from Ca and Sr exchange reactions and Sr isotopic ratios. *Journal of Geophysical Research*, 93, 4573–4583.

Berndt, M. E., & Seyfried Jr., W. E. (1990). Boron, bromine, and other trace elements as clues to the fate of chlorine in mid-ocean ridge vent fluids. *Geochimica et Cosmochimica Acta,* 54, 2235–2245.

Besson, P., Degboe, J., Berge, B., Chavagnac, V., Fabre, S., & Berger, G. (2014). Calcium, Na, K and Mg Concentrations in Seawater by Inductively Coupled Plasma-Atomic Emission Spectrometry: Applications to IAPSO Seawater Reference Material, Hydrothermal Fluids and Synthetic Seawater Solutions. *Geostandards and Geoanalytical Research,* 38, 355–362. doi:10.1111/j.1751-908X.2013.00269.x.

Brant, C., Coogan, L. A., Gillis, K. M., Seyfried Jr., W. E., Pester, N. J., & Spence, J. (2012). Lithium and Li-isotopes in young altered upper oceanic crust from the East Pacific Rise. *Geochimica et Cosmochimica Acta,* 96, 272–293. doi:10.1016/j.gca.2012.08.025.

Caine, J. S., Bruhn, R. L., & Forster, C. B. (2010). Internal structure, fault rocks, and inferences regarding deformation, fluid flow, and mineralization in the seismogenic stillwater normal fault, Dixie Valley, Nevada. *Journal of Structural Geology*, 32(11), 1576–1589, doi:10.1016/j.jsg.2010.03.004.

525 Campbell, A. C., Bowers, T. S., Measures, C. I., Falkner, K. K., Khadem, M., & Edmond, J.
526 (1988). A time series of vent fluid compositions from 21°N, East Pacific Rise (1979, 1981,
527 1985), and the Guaymas Basin, Gulf of California (1982, 1985). *Journal of Geophysical*
528 *Research - Solid Earth*, 93, 4537–4549.

529 Cannat, M., Briais, A., Deplus, C., Escartin, J., Georgen, J., Lin, J., et al. (1999). Mid-Atlantic-
530 Azores hotspot interactions: along-axis migration of a hotspot-derived event of enhanced
531 magmatism 10 to 4 Ma ago. *Earth and Planetary Science Letters,* 173, 257–269.

532 Charlou, J. L., Donval, J. P., Douville, E., Jean-Baptiste, P., Radford-Knoery, J., Fouquet, Y.,
533 et al. (2000). Compared geochemical signatures and the evolution of Menez Gwen (37°50'N)
534 and Lucky Strike (37°17'N) hydrothermal fluids, south of the Azores Triple Junction on the
535 Mid-Atlantic Ridge. *Chemical Geology,* 171, 49–75.

536 Chavagnac, V., Leleu, T., Boulart, C., Barreyre, T., Castillo, A., Menjot, L., et al. (2015). Deep-
537 Sea Observatory EMSO-Azores (Lucky Strike, 37°17'N MAR): Impact of Fluid Circulation
538 Pathway on Chemical Hydrothermal Fluxes, in *Follow the Fluids: Integrating*
539 *Multidisciplinary Observations of Deep-Sea Hydrothermal Systems II.*, AGU Fall Meeting, San
540 Francisco.

541 Chavagnac, V., Saleban Ali, H., Jeandel, C., Leleu, T., Destrigneville, C., Castillo, A., et al.,
542 (2018). Sulfate minerals control dissolved rare earth element flux and Nd isotope signature of
543 buoyant hydrothermal plume (EMSO-Azores, 37°N Mid-Atlantic Ridge). *Chemical Geology,*
544 doi:10.1016/j.chemgeo.2018.09.021

545 Chen, Y., & Morgan, W. J. (1990). A Nonlinear Rheology Model for Mid-Ocean Ridge Axis
546 Topography. *Journal of Geophysical Research,* 95, 17583–17604.

547 Colaço, A., Blandin, J., Cannat, M., Carval, T., Chavagnac, V., Connelly, D. P., et al. (2011).
548 MoMAR-D: a technological challenge to monitor the dynamics of the Lucky Strike vent
549 ecosystem. *ICES Journal of Marine Science,* 68, 416–424. doi:10.1093/icesjms/fsq075.

550 Combier, V., Seher, T., Singh, S. C., Crawford, W. C., Cannat, M., Escartín, J., & Dusunur D.
551 (2015). Three-dimensional geometry of axial magma chamber roof and faults at Lucky Strike
552 volcano on the Mid-Atlantic Ridge: Magma chamber and faulting at Lucky Strike. *Journal of*
553 *Geophyical Research- Solid Earth,* 120, 5379–5400. doi:10.1002/2015JB012365.

554 Coogan, L. A. (2008). Reconciling temperatures of metamorphism, fluid fluxes, and heat
555 transport in the upper crust at intermediate to fast spreading mid-ocean ridges. *Geochemistry,*
556 *Geophysics, Geosystems*, 9(3), doi:10.1029/2007GC001787.

557 Coumou, D., Driesner, T., Weis, P., & Heinrich, C. A. (2009). Phase separation, brine
558 formation, and salinity variation at Black Smoker hydrothermal systems. *Journal of*
559 *Geophysical Research,* 114, doi:10.1029/2008JB005764.

560 Crawford, W. C., Rai, A., Singh, S. C., Cannat, M., Escartin, J., Wang, H., et al. (2013).
561 Hydrothermal seismicity beneath the summit of Lucky Strike volcano, Mid-Atlantic Ridge.
562 *Earth and Planetary Science Letters,* 373, 118–128. doi:10.1016/j.epsl.2013.04.028.

563 Delaney, J. R., Mogk, D. W., & Mottl, M. J. (1987). Quartz-Cemented Breccias From the Mid-
564 Atlantic Ridge: Samples of a High-Salinity Hydrothermal Upflow Zone. *Journal of Geophyical*
565 *Research,* 92, 3767-3787.

566 Douville, E., Charlou, J. L., Oelkers, E. H., Bienvenu, P., Jove Colon, C. F., Donval, J. P., et
567 al. (2002). The rainbow vent fluids (36 14′ N, MAR): the influence of ultramafic rocks and
568 phase separation on trace metal content in Mid-Atlantic Ridge hydrothermal fluids. *Chemical*
569 *Geology,* 184, 37–48.

570 Driesner, T. (2007). The system $H_2O$–NaCl. Part II: Correlations for molar volume, enthalpy,
571 and isobaric heat capacity from 0 to 1000°C, 1 to 5000bar, and 0 to 1 XNaCl. *Geochimica et*
572 *Cosmochimica Acta,* 71, 4902–4919, doi:10.1016/j.gca.2007.05.026.

573 Driesner, T., & Heinrich, C. A. (2007). The system $H_2O$–NaCl. Part I: Correlation formulae for
574 phase relations in temperature–pressure–composition space from 0 to 1000°C, 0 to 5000bar,
575 and 0 to 1 XNaCl. *Geochimica et Cosmochimica Acta, 71*, 4880–4901,
576 doi:10.1016/j.gca.2006.01.033.

577 Elderfield, H., & Schultz, A. (1996). Mid-ocean ridge hydrothermal fluxes and the chemical
578 composition of the ocean. *Annual Review of Earth Planetary Sciences*, 24, 191–224.

579 Escartin, J., Barreyre, T., Cannat, M., Garcia, R., Gracias, N., Deschamps, A., et al. (2015).
580 Hydrothermal activity along the slow-spreading Lucky Strike ridge segment (Mid-Atlantic
581 Ridge): Distribution, heatflux, and geological controls. *Earth and Planetary Science Letters,*
582 431, 173–185, doi:10.1016/j.epsl.2015.09.025.

583 Fontaine, F. J., & Wilcock, W. S. D. (2006). Dynamics and storage of brine in mid-ocean ridge
584 hydrothermal systems. *Journal of Geophysical Research,* 111, doi:10.1029/2005JB003866.

585 Fontaine, F. J., Wilcock, W. S. D., & Butterfield, D. A. (2007). Physical controls on the salinity
586 of mid-ocean ridge hydrothermal vent fluids. *Earth and Planetary Science Letters,* 257, 132–
587 145, doi:10.1016/j.epsl.2007.02.027.

588 Fontaine, F. J., Wilcock, W. S. D., Foustoukos, D. I., & Butterfield, D. A. (2009). A Si-Cl
589 geothermobarometer for the reaction zone of high-temperature, basaltic-hosted mid-ocean ridge
590 hydrothermal systems: Si/Cl-inferred P–T in MOR hydrothermal systems. *Geochemistry,*
591 *Geophysics, Geosystems,* 10, doi:10.1029/2009GC002407.

592 Fouquet, Y., Ondréas, H., Charlou, J. L., Donval, J. P., & Radford-Knoery, J. (1995). Atlantic
593 lava lakes and hot vents. *Nature,* 377, 201, doi:10.1038/377201a0.

594 Foustoukos, D. I., & Seyfried Jr., W. E. (2007a). Trace element partitioning between vapor,
595 brine and halite under extreme phase separation conditions. *Geochimica et Cosmochimica Acta,*
596 71, 2056–2071, doi:10.1016/j.gca.2007.01.024.

597 Foustoukos, D. I., & Seyfried Jr., W. E. (2007b). Quartz solubility in the two-phase and critical
598 region of the NaCl–KCl–H2O system: Implications for submarine hydrothermal vent systems
599 at 9°50′N East Pacific Rise. *Geochimica et Cosmochimica Acta,* 71, 186–201,
600 doi:10.1016/j.gca.2006.08.038.

601 Goldfarb, M. S., & Delaney, J. R. (1998). Response of Two-Phase Fluids to Fracture
602 Configurations Within Submarine Hydrothermal Systems. *Journal of Geophysical Research,*
603 *93*(B5), 4585-4594.

604 Hamelin, C., Bezos, A., Dosso, L., Escartin, J., Cannat, M., & Mevel, C. (2013). Atypically
605 depleted upper mantle component revealed by Hf isotopes at Lucky Strike segment. *Chemical*
606 *Geology,* 341, 128–139, doi:10.1016/j.chemgeo.2013.01.013.

607 Heft, K. L., Gillis, K. M., Pollock, M. A., Karson, J. A., & Klein, E. M. (2008). Role of
608 upwelling hydrothermal fluids in the development of alteration patterns at fast spreading ridges:
609 Evidence from the sheeted dike complex at Pito Deep. *Geochemistry, Geophysics, Geosystems,*
610 9, 1-21.

611 Honnorez, J. (2003). Hydrothermal alteration vs. ocean-floor metamorphism. A comparison
612 between two case histories: the TAG hydrothermal mound (Mid-Atlantic Ridge) vs.
613 DSDP/ODP Hole 504B (Equatorial East Pacific). *Comptes Rendus Géoscience,* 335, 781-824,
614 doi: 10.1016/j.crte.2003.08.009.

615 Humphris, S. E., Fornari, D. J., Scheirer, D. S., German, C. R., & Parson, L. M. (2002).
616 Geotectonic setting of hydrothermal activity on the summit of Lucky Strike Seamount
617 (37°17′N, Mid-Atlantic Ridge): Geotectonic setting. *Geochemistry, Geophysics, Geosystems,*
618 3, 1–25, doi:10.1029/2001GC000284.

619 James, R. H., Elderfield, H., & Palmer M. R. (1995). The chemistry of hydrothermal fluids
620 from the Broken Spur site, 29°N Mid-Atlantic Ridge. *Geochimica et Cosmochimica Acta,* 59,
621 651–659.

622 Jupp, T., & Schultz, A. (2000). A thermodynamic explanation for black smoker temperatures.
623 *Nature*, 403:6772, 880-883. doi:10.1038/35002552.

624 Kelley, D. S., & Delaney, J. R. (1987). Two-phase separation and fracturing in mid-ocean ridge
625 gabbros at temperatures greater than 700°C. *Earth and Planetary Science Letters,* 83, 53–66.

626 Kelley, D. S., & Robinson, P. T. (1990). Development of a brine-dominated hydrothermal
627 system at temperatures of 400–500 C in the upper level plutonic sequence, Troodos ophiolite,
628 Cyprus. *Geochimica et Cosmochimica Acta*, 54, 653–661.

629 Langmuir, C., Humphris, S. E., Fornari, D. J., Van Dover, C., Von Damm, K. L., Tivey, D.
630 Colodner, M. K., et al. (1997). Hydrothermal vents near a mantle hot spot: the Lucky Strike
631 vent field at 37°N on the Mid-Atlantic Ridge. *Earth and Planetary Science Letters,* 148, 69–
632 91.

633 Larson, B. I., Lilley, M. D., & Olson, E. J. (2009). Parameters of subsurface brines and
634 hydrothermal processes 12-15 months after 1999 magmatic event at the Main Endeavor Field
635 as inferred from in situ time series measurements of Chloride and Temperature. *Journal of*
636 *Geophysical Research*, 114(B01207), 1-18, doi: 10.1029/2008JB005627.

637 Lowell, R. P. (2003). Anhydrite precipitation and the relationship between focused and diffuse
638 flow in seafloor hydrothermal systems. *Journal of Geophysical Research,* 108,
639 doi:10.1029/2002JB002371.

640 Ludwig, K. A., Kelley, D. S., Butterfield, D. A., Nelson, B. K., & Früh-Green, G. (2006).
641 Formation and evolution of carbonate chimneys at the Lost City Hydrothermal Field.
642 *Geochimica et Cosmochimica Acta,* 70, 3625–3645, doi:10.1016/j.gca.2006.04.016.

643 Martin, W., Baross, J., Kelley, D., & Russell, M. J. (2008). Hydrothermal vents and the origin
644 of life. *Natural Review of Microbiology,* doi:10.1038/nrmicro1991.

645 Millero, F. J., Feistel, R., Wright, D. G., & McDougall, T. J. (2008). The composition of
646 Standard Seawater and the definition of the Reference-Composition Salinity Scale. *Deep Sea*
647 *Research,* 55, 50–72, doi:10.1016/j.dsr.2007.10.001.

648 Miranda, J. M., Luis, J. F., Lourenço, N., & Santos, F. M. (2005). Identification of the
649 magnetization low of the Lucky Strike hydrothermal vent using surface magnetic data:
650 magnetization low of Lucky Strike. *Journal of Geophysical Research-Solid Earth,* 110,
651 doi:10.1029/2004JB003085.

652 Mottl, M. J., Seewald, J. S., Wheat, C. G., Tivey, M. K., Michael, P. J., Proskurowski, G., et al.
653 (2011). Chemistry of hot springs along the Eastern Lau Spreading Center. *Geochimica et*
654 *Cosmochimica Acta,* 75, 1013–1038, doi:10.1016/j.gca.2010.12.008.

655 Ondréas, H., Cannat, M., Fouquet, Y., Normand, A., Sarradin, P. M., & Sarrazin, J. (2009).
656 Recent volcanic events and the distribution of hydrothermal venting at the Lucky Strike
657 hydrothermal field, Mid-Atlantic Ridge: Lucky Strike volcanism and venting. *Geochemistry,*
658 *Geophysics, Geosystems,* 10, doi:10.1029/2008GC002171.

659 Palmer, M. R. (1992). Controls over the chloride concentration of submarine hydrothermal vent
660 fluids: evidence from Sr/Ca and $^{87}Sr/^{86}Sr$ ratios. *Earth and Planetary Science Letters,* 109, 37–
661 46.

662 Person, R., Miranda, J. M., & Puillat, I. (2009). ESONEWS-MoMAR/DA demonstration
663 mission to establish a multidisciplinary observatory at hydrothermal vents on the Mid-Atlantic
664 Ridge. *Esonews,* 3, 1–8.

665 Pester, N. J., Rough, M., Ding, K., & Seyfried Jr., W. E. (2011). A new Fe/Mn geothermometer
666 for hydrothermal systems: Implications for high-salinity fluids at 13°N on the East Pacific Rise.
667 *Geochimica et Cosmochimica Acta,* 75, 7881–7892, doi:10.1016/j.gca.2011.08.043.

668 Pester, N. J., Reeves, E. P., Rough, M. E., Ding, K., Seewald, J. S., & Seyfried Jr., W. E. (2012).
669 Subseafloor phase equilibria in high-temperature hydrothermal fluids of the Lucky Strike
670 Seamount (Mid-Atlantic Ridge, 37°17′N). *Geochimica et Cosmochimica Acta,* 90, 303–322,
671 doi:10.1016/j.gca.2012.05.018.

672 Pester, N. J., Ding, K., & Seyfried Jr., W. E. (2015). Vapor–liquid partitioning of alkaline earth
673 and transition metals in NaCl-dominated hydrothermal fluids: An experimental study from 360
674 to 465°C, near-critical to halite saturated conditions. *Geochimica et Cosmochimica Acta*, 168,
675 111–132, doi:10.1016/j.gca.2015.07.028.

676 Pokrovski, G. S., Roux, J., & Harrichoury, J. C. (2005). Fluid density control on vapor-liquid
677 partitioning of metals in hydrothermal systems. *Geology,* 33, 657–660.

678 Ravizza, G., Blusztajn, J., Von Damm, K. L., Bray, A. M., Bach, W., & Hart, S. R. (2001). Sr
679 isotope variations in vent fluids from 9° 46′-9° 54′ N East Pacific Rise: evidence of a non-zero-
680 Mg fluid component. *Geochimica et Cosmochimica Acta,* 65, 729–739.

Reeves, E. P., Seewald, J. S., Saccocia, P., Bach, W., Craddock, P. R., Shanks, W. C., et al. (2011). Geochemistry of hydrothermal fluids from the PACMANUS, Northeast Paul and Vienna Woods hydrothermal fields, Manus Basin, Papua New Guinea. *Geochimica et Cosmochimica Acta,* 75, 1088–1123, doi:10.1016/j.gca.2010.11.008.

Resing, J. A., Sedwick, P. N., German, C. R., Jenkins, W. J., Moffett, J. W., Sohst, B. M., & Tagliabue, A. (2015). Basin-scale transport of hydrothermal dissolved metals across the South Pacific Ocean. *Nature,* 523, 200–203, doi:10.1038/nature14577.

Saccocia, P. J., & Seyfried Jr., W. E. (1994). The solubility of chlorite solid solutions in 3.2 wt% NaCl fluids from 300–400 °C, 500 bars. *Geochimica et Cosmochimica Acta,* 58, 567–585.

Schmidt, K., Koschinsky, A., Garbeschonberg, D., Decarvalho, L., & Seifert, R. (2007). Geochemistry of hydrothermal fluids from the ultramafic-hosted Logatchev hydrothermal field, 15°N on the Mid-Atlantic Ridge: Temporal and spatial investigation. *Chemical Geology,* 242, 1–21, doi:10.1016/j.chemgeo.2007.01.023.

Schmidt, K., Garbe-Schönberg, D., Koschinsky, A., Strauss, H., Jost, C. L., Klevenz, V., & Königer, P. (2011). Fluid elemental and stable isotope composition of the Nibelungen hydrothermal field (8°18′S, Mid-Atlantic Ridge): Constraints on fluid–rock interaction in heterogeneous lithosphere. *Chemical Geology,* 280, 1–18, doi:10.1016/j.chemgeo.2010.07.008.

Seewald, J. S., & Seyfried Jr., W. E. (1990). The effect of temperature on metal mobility in subseafloor hydrothermal systems: constraints from basalt alteration experiments. *Earth and Planetary Science Letters,* 101, 388–403.

Seyfried Jr., W. E. (2003). Chemistry of hydrothermal vent fluids from the Main Endeavour Field, northern Juan de Fuca Ridge: Geochemical controls in the aftermath of June 1999 seismic events. *Journal of Geophysical Research,* 108, doi:10.1029/2002JB001957.

Seyfried Jr., W. E., Chen, X., & Chan, L. H. (1998). Trace element mobility and lithium isotope exchange during hydrothermal alteration of seafloor weathered basalt: an experimental study at 350 C, 500 bars. *Geochimica et Cosmochimica Acta,* 62, 949–960.

Singh, S. C., Crawford, W. C., Carton, H., Seher, T., Combier, V., Cannat, M., et al. (2006). Discovery of a magma chamber and faults beneath a Mid-Atlantic Ridge hydrothermal field. *Nature,* 442, 1029–1032, doi:10.1038/nature05105.

Steele-MacInnis, M., Han, L., Lowell, R. P., Rimstidt, J. D., & Bodnar, R. J. (2012). The role of fluid phase immiscibility in quartz dissolution and precipitation in sub-seafloor hydrothermal systems. *Earth and Planetary Science Letters,* 321-322, 139–151, doi:10.1016/j.epsl.2011.12.037.

Stein, C. A., & Stein, S. (1994). Constraints on hydrothermal heat flux through the oceanic lithosphere from global heat flow. *Journal of Geophysical Research-Solid Earth,* 99, 3081–3095.

Von Damm, K. L. (1988). Systematics and postulated controls on submarine hydrothermal solution chemistry. *Journal of Geophysical Research-Solid Earth,* 93, 4551–4561.

Von Damm, K. L. (2000). Chemistry of hydrothermal vent fluids from 9–10 N, East Pacific Rise: "Time zero," the immediate post-eruptive period. *Journal of Geophysical Research-Solid Earth,* 105, 11203–11222.

Von Damm, K. L., Bischoff, J., & Rosenbauer, R. J. (1991). Quartz solubility in hydrothermal seawater: an experimental study and equation describing quartz solubility for up to 0.5M NaCl solutions. *American Journal of Science,* 291, 997–1007.

725 Von Damm, K. L., Bray, A. M., Buttermore, L. G., & Oosting, E. S. (1998). The geochemical
726 controls on vent fluids from the Lucky Strike vent field, Mid-Atlantic Ridge. *Earth and*
727 *Planetary Science Letters,* 160, 521–536.

728 Von Damm, K. L., Lilley, M. D., Shanks III, W. C., Brockington, M., Bray, A. M., O'Grady,
729 K. M., et al. (2003). Extraordinary phase separation and segregation in vent fluids from the
730 southern East Pacific Rise. *Earth and Planetary Science Letters,* 206, 365–378.

731

**Figure 1.** Bathymetric map of the Lucky Strike central volcano. Active hydrothermal vents are reported. Violet star: SW group composed of Sapins (Sa), Crystal (Cr) and South Crystal (SCr); Yellow star: SE group composed of Tour Eiffel (TE), Aisics (Ai) and Montsegur (MS); Green star: NE group composed of Sintra (Si) and Y3; Black star: Central group composed of Cyprès (Cy), White Castle (WC) and Isabel (Is); The red star locates Capelinhos (Cap). See text for details. Microbathymetry from Ondréas et al. (2009).

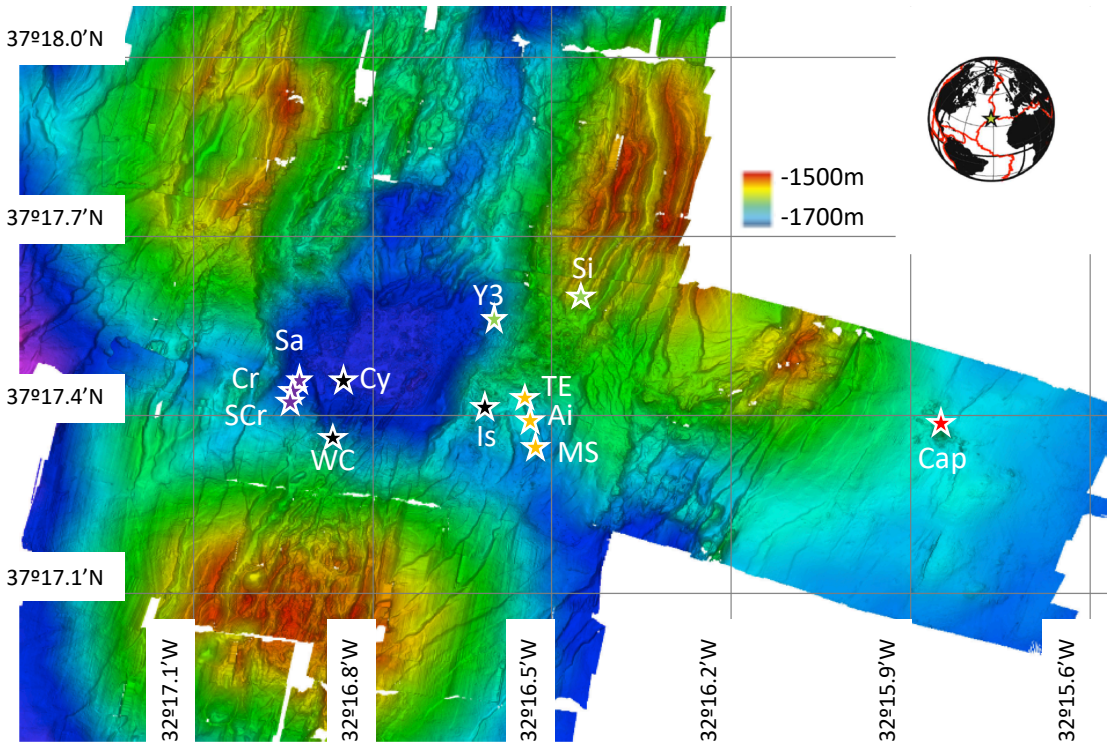


**Figure 2.** Overview of vent morphology. Snapshots of ROV videos (Ifremer-CNRS, MoMARsat 13), a), b) Capelinhos; c) Aisics; d) Montsegur; e) Cyprès; f) White Castle; g) Crystal; h) Sintra. a) and b) show candelabra-like structures that discharge focused high T fluid at Capelinhos vent site. c) and d) show hydrothermal mounds in the South Eastern hydrothermal area. The Aisics mound (c) is not as developed as the Montsegur mound (d) but both lack of tall indurated chimneys. e), f) and g) are situated in the South Western hydrothermal area. There, high-T vents are commonly set on elongated wall-like structures related to underlying

fissures. h) is situated in the waning North Eastern hydrothermal area and shows tall indurated chimneys which are probably inherited from past intense activity.

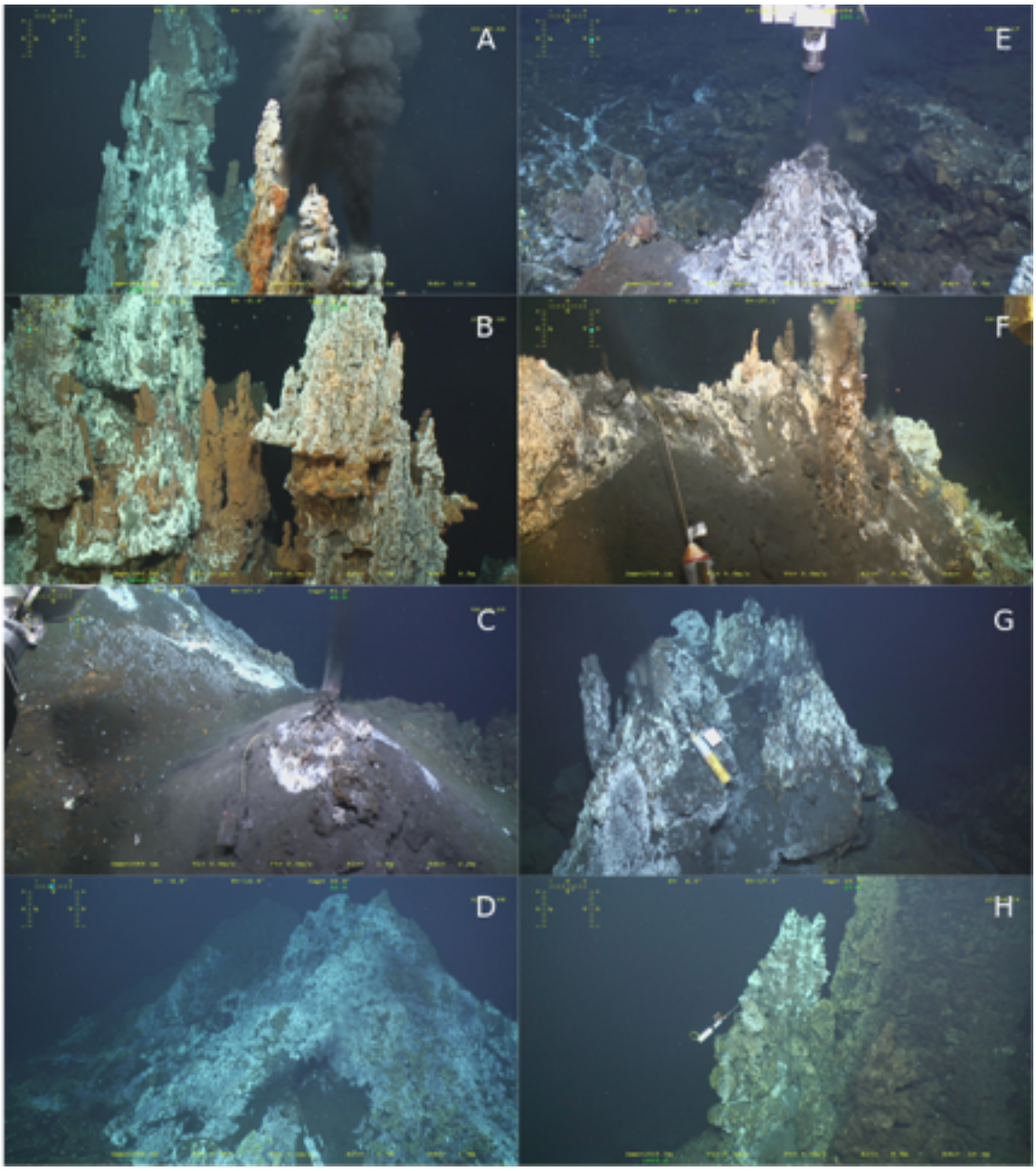

749 **Figure 3.** Fe, Mn and Si vs. Cl. in end-member fluids a) Fe versus Cl; b) Mn and versus Cl and

750 c) Si versus Cl. These diagrams show the lack of correlation of these elements relative to Cl.

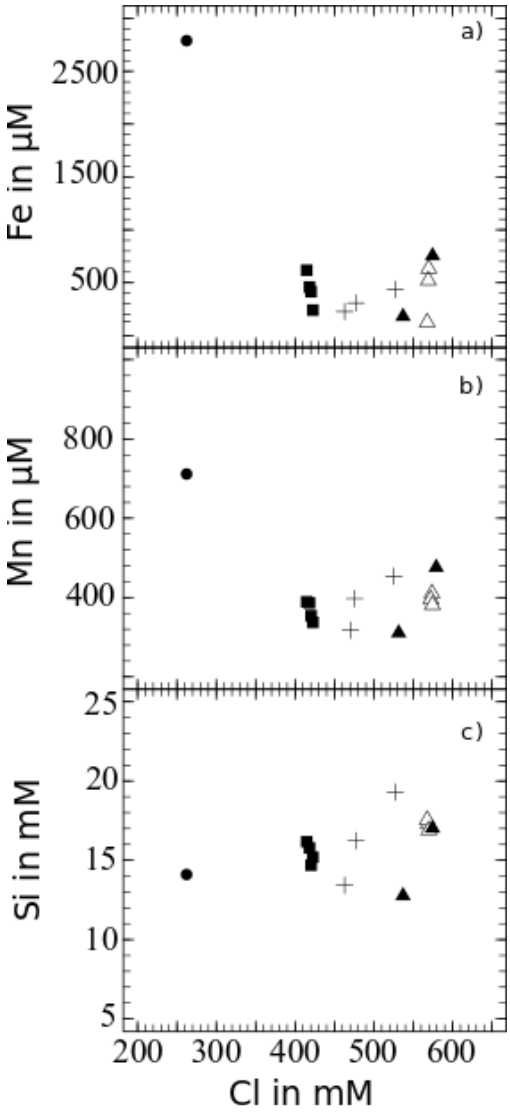


751

752

753 **Figure 4.** log (Elt/Cl) vs log (Cl) diagram. Diagram of elt/Cl versus Cl showing the linear
754 relationship between trace element and chlorinity, a proxy for the effect of phase separation.

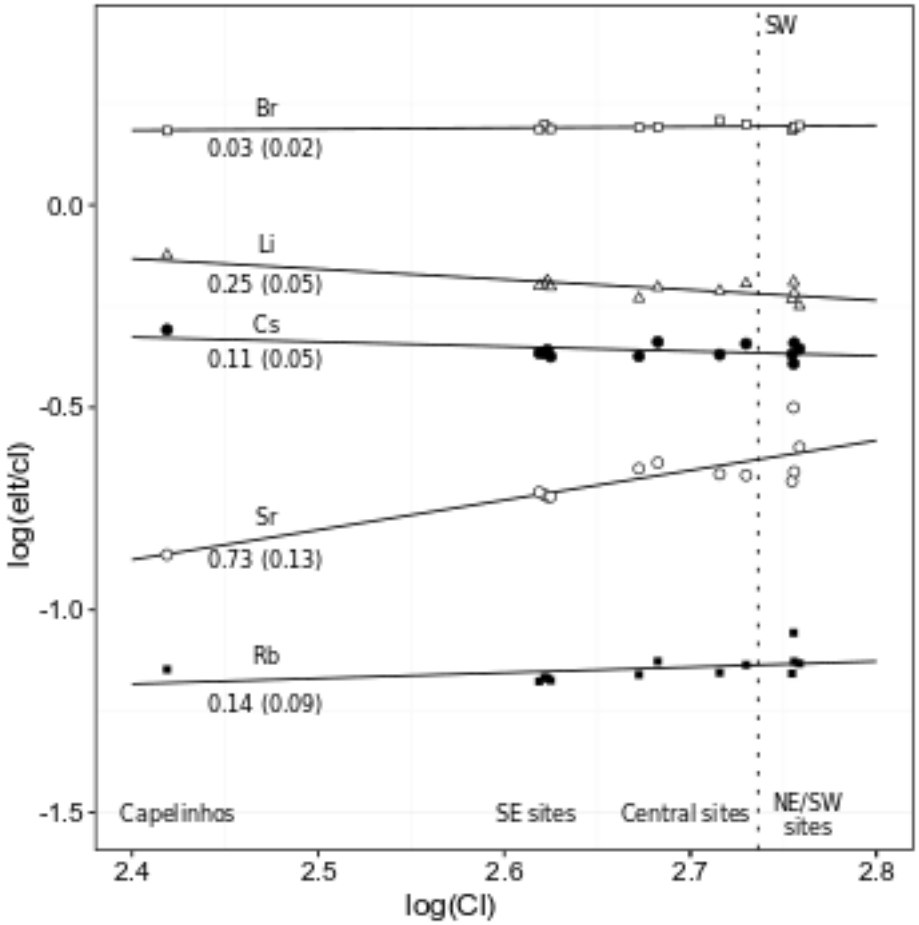


755

756

**Figure 5.** Geochemical information for P and T. a) Quartz geothermobarometer based on Foustoukos and Seyfried (2007b). Points represent Si measured in fluids with calculated temperature based on the Fe-Mn geothermometer. Grey dashed lines represent the "classical" approach to evaluate P and T (see text for details). b) Fe and Mn concentrations on a logarithm scale (Modified from Pester et al., 2011). Grey line represent basalt alteration line and black dashed lines are isotherms calculated from the Fe/Mn geothermometer.

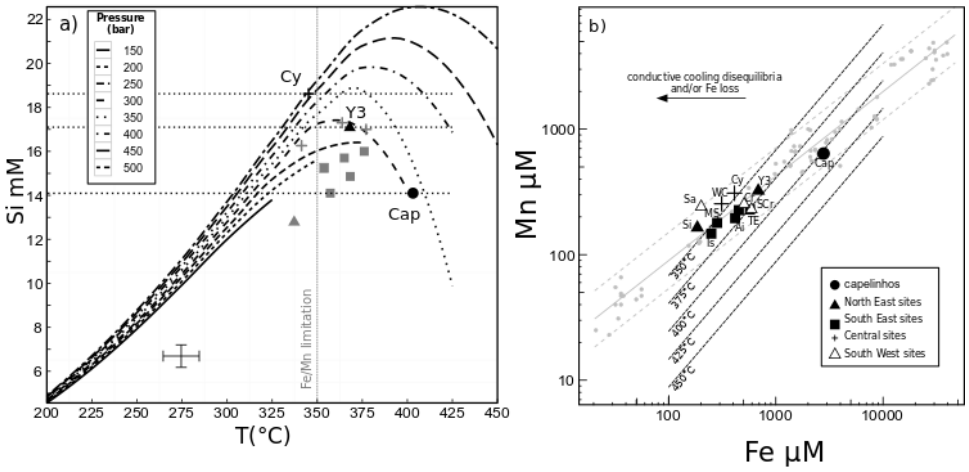


**Figure 6.** Fluid circulation. a) Calculated P and T of some vents at equilibria with quartz are presented. P and T were calculated using the Fe/Mn geothermometer of Pester et al. (2011), quartz geothermobarometer (Foustoukos & Seyfried, 2007b) and NaCl-$H_2O$ solution properties (Driesner et al., 2007) (See details in text). Dotted lines represent the depth of the base of layer 2A for western and eastern sites (Arnulf et al., 2011). The red shaded domain represents the range of depth to the top of the axial magma chamber as identified by Singh et al. (2006) and Combier et al. (2015). Grey lines represent fault labeled F1, F1b in Combier et al. (2015), dotted grey line correspond to F2. The blue line represents the inferred P–T path in the recharge zone where cold seawater percolate through oceanic crusts and gradually interacts with rocks. Red lines represent the inferred P–T path in the upflow zone, based on the conditions estimated from fluid chemistry. The grey rectangle represents the phase separation zone estimated from the Si and Cl concentrations in the low salinity fluids (Capelinhos, TE) using the geothermobarometer

776 proposed by Fontaine et al. (2009). b) Modified from Escartin et al. (2015). Cartoon
777 representing the hydrothermal cell under the LSHF. Blue arrows represent downward flow of
778 seawater; red arrows are focused hot fluid moving upward through cracks and faults. Black star
779 represents the hypothetic position of Capelinhos fluid extraction through a high angle fault.
780 Seismic clusters are from Crawford et al. (2013). F1, F1b and F2 from Combier et al. (2015).

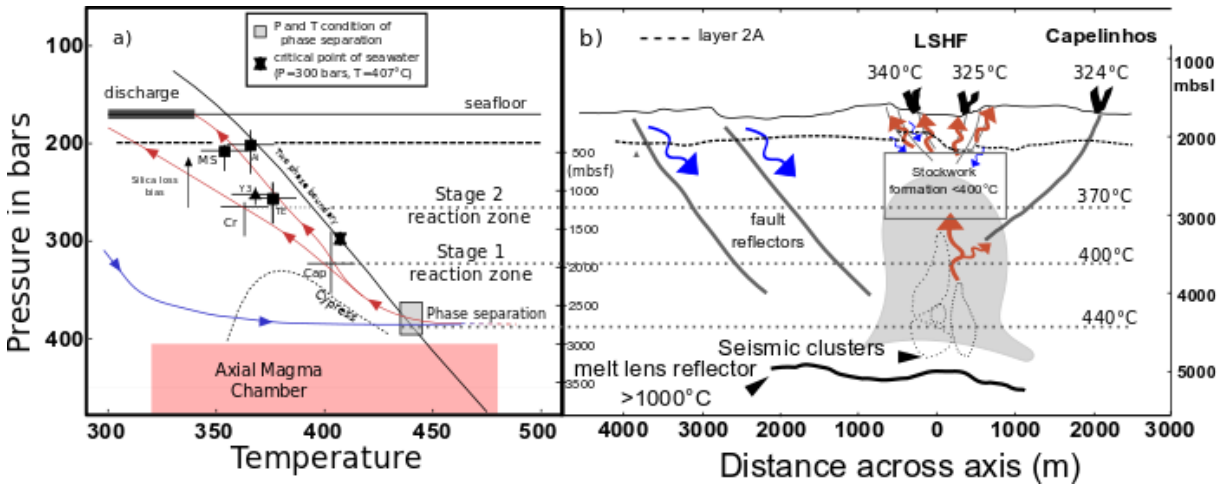

781

782

783 **Table 1.** Summary of fluid sampling. The table presents location, depth and details on fluid
784 sampling for each site (minimum pH, minimum Mg measured and corresponding seawater
785 entrainment, and maximum temperature measured in the vent prior to sampling).

| site | depth (mbsl) | Longitude (W) | Latitude (N) | Hydrothermal Group | pH_ | Mg (mM)# | n sample | %SW * | T in situ (ºC) |
|---|---|---|---|---|---|---|---|---|---|
| Capelinhos | 1665 | 32º15.830' | 37º17.350' | Capelinhos | 2,56 | 1,63 | 4 | 3,02 | 324 |
| Aisics | 1689,3 | 32º16.530' | 37º17.338' | South-East | 3,1 | 1,11 | 7 | 2,06 | 295 |
| Tour Eiffel | 1684 | 32º16.532' | 37º17.343' | South-East | 3,26 | 0,89 | 3 | 1,65 | 325 |
| Montségur | 1701 | 32º16.534 | 37º17.284' | South-East | 3,33 | 1,63 | 2 | 3,02 | 316 |
| Cyprès | 1738,7 | 32º16.863' | 37º17.450' | Central | 2,84 | 1,53 | 3 | 2,84 | 304 |
| Isabel | 1683,7 | 32º16.638' | 37º17.377' | Central | 2,93 | 1,55 | 3 | 2,87 | 224 |
| White Castle | 1708,9 | 32º16.869' | 37º17.383' | Central | 2,9 | 1,18 | 3 | 2,18 | 317 |
| Crystal | 1723,3 | 32º16.921' | 37º17.453' | South-West | 3,17 | 1,61 | 2 | 2,98 | 335 |
| Sapins | 1718,6 | 32º16.888' | 37º17.439' | South-West | 3,56 | 3,6 | 3 | 6,67 | 280 |
| South Crystal | 1720,5 | 32º16.935' | 37º17.445' | South-West | 2,93 | 0,75 | 3 | 1,39 | 340 |
| Sintra | 1614,7 | 32º16.498' | 32º17.529' | North-East | 3,89 | 12,99 | 1 | 24,06 | 196 |
| Y3 | 1727,3 | 32º16.671' | 37º17.512' | North-East | 2,92 | 1,06 | 3 | 1,97 | 325 |

_: on-board pH measurement at ambient temperature
#: minimum Mg measured on samples for each site
786 *: calculated from Mg concentration

787 **Table 2.** End-member composition of fluids from the LSHF. The concentration of end-member
788 fluids for each site is calculated based on linear least-square regression of element vs. Mg, at
789 Mg=0 (Albarède et al., 1981; Ravizza et al., 2001; Fig S1).

| site | group | Ca mM | K mM | Na mM | Fe µM | Mn µM | Si mM | Cl mM | SO4 mM | Br mM | Rb µM | Sr µM | Li µM | Cs µM | 87Sr/86Sr | T** | P** |
|---|---|---|---|---|---|---|---|---|---|---|---|---|---|---|---|---|---|
| Capelinhos | Cap | 17.97±0.16 | 12.1±0.3 | 205.0±1.7 | 2789.4±84.8 | 639.5±27.6 | 14.1±1.1 | 262.3±0.1 | -0.4±0.04 | 0.40±0.02 | 18.7±0.3 | 35.89±0.65 | 197.3±0.3 | 0.129±0.003 | 0,70384 | 403 | 350 |
| Aisics | SE | 35.46±1.44 | 19.6±0.6 | 309.7±19.7 | 417.6±8.0 | 195.3±4.0 | 14.86±0.12 | 419.9±1.8 | 0.11±0.23 | 0.65±0.01 | 28.5±0.1 | 80.06±0.38 | 272.9±0.3 | 0.184±0.07 | 0,70422 | 368 | 225 |
| Aisics | SE | 37.25±0.12 | 19.0±0.1 | 316.8±1.1 | 452.03±10.24 | 226.3±4.86 | 15.7±0.12 | 418.4±1.1 | 0.02±0.07 | 0.66±0.04 | 28.5±0.2 | 80.5±0.7 | 266.3±0.4 | 0.18±0.001 | 0,70428 | 365 | n.d. |
| Montségur | SE | 36.13±.46 | 19.6±0.1 | 325.3±0.8 | 283.7±20.7 | 179.2±8.4 | 15.25±0.04 | 421.7±1.3 | -0.06±0.03 | 0.65±0.02 | 28.3±0.03 | 80.3±1.1 | 265±0.4 | 0.179±0.002 | 0,70423 | 354 | 225 |
| Tour Eiffel | SE | 39±0.64 | 19.7±0.4 | 334.4±6.5 | 574±68.19 | 229±15.51 | 15.1±0.82 | 415.7±4.7 | 0.9±1.29 | 0.64±0.02 | 27.7±1.3 | 81.16±0.53 | 262.6±0.4 | 0.179±0.008 | 0,70448 | 376 | 300 |
| Cyprès | Central | 43.24±0.03 | 23.4±0.1 | 399.34±2.2 | 411.33±16.64 | 309.01±11.58 | 18.62±0.27 | 519.7±2.7 | -0.48±0.08 | 0,84±0.01 | 36.37±0.47 | 112.47±0.77 | 319±0.3 | 0.222±0.074 | 0,70403 | 345 | n.d. |
| Isabel | Central | 39.6±0.37 | 22.3±0.2 | 373.8±5.7 | 250.42±21.29 | 147.05±1.92 | 14.1±0.3 | 470.3±11.2 | -0.2±0.31 | 0.73±0.01 | 32.56±1.39 | 105.0±4.3 | 276.8±04 | 0.199±0.004 | 0,7043 | 357 | n.d. |
| White Castle | Central | 38.35±0.11 | 23.2±0.1 | 381.8±1.4 | 312.7±11.37 | 254.44±16.34 | 16.26±0.11 | 481.4±2.5 | -0.2±0.01 | 0.75±0.01 | 35.95±0.1 | 111.19±0.28 | 301.6±0.1 | 0.221±0.003 | 0,70502 | 341 | n.d. |
| Crystal | SW | 53,55±3.9 | 28.4±0.1 | 445,9±0.4 | 507±68.55 | 260±19.4 | 17.3±0.77 | 569,5±0.3 | 2,56±2.69 | 0,88±0.01 | 50±5.65 | 180±45.85 | 367.9±0.3 | 0.231±0.004 | 0,70414 | 364 | 300 |
| South Crystal | SW | 49.3±0.8 | 28.3±0.1 | 445±1.5 | 593.4±31.7 | 231.8±10.04 | 17±0.12 | 569.9±1.3 | 0.1±0.02 | 0.89±0.05 | 42.5±0.11 | 125±0.42 | 346.1±0.4 | 0.260±0.004 | 0,704 | 377 | 300 |
| Sapins | SW | 48.3±0.72 | 26.6±0.3 | 441.8±4.7 | 201.7±21.6 | 245.4±14.45 | 17.5±0.45 | 568.4±8.8 | -0.28±0.97 | 0.87±0.01 | 39.6±0.87 | 118.1±2.36 | 332.9±.5 | 0.243±0.005 | 0,70429 | 322 | n.d. |
| Sintra | NE | 53.7 | 27.1 | 433.2 | 185.5 | 164.1 | 12.8 | 537 | 0.35 | 0.85 | 39.3 | 115.5 | 343.5 | 0.244 | 0.70423 | 337 | n.d. |
| Y3 | NE | 52.9±0.5 | 25.5±0.4 | 432.0±4.5 | 686.7±11.3 | 323.0±18.0 | 17.1±0.2 | 573.7±8.5 | 0.03±0.12 | 0.90±0.01 | 42.3±0.05 | 144.7±0.6 | 323.3±0.3 | 0.253±0.001 | 0,70401 | 368 | 300 |
| Seawater | | 10.31 | 9.8 | 464 | 0 | 0 | 0.17 | 545 | 28.3 | 0.84 | 2.0 | 87.0 | 25.6 | | 0,70916 | | |

**: Temperature calculated by the Fe/Mn geothermometer and pressure estimated from Fe/Mn and Si concentrations (see text for details)
n.d. : not determined

790

Supporting information for

# Spatial Variations in Vent Chemistry at the Lucky Strike Hydrothermal Field, Mid Atlantic Ridge (37°N): Updates for Subseafloor Flow Geometry from the Newly Discovered Capelinhos Vent.

**V. Chavagnac[1], T. Leleu[1], F. Fontaine[2,3], M. Cannat[2], G. Ceuleneer[1], A. Castillo[1]**

[1] Geosciences Environnement Toulouse, Université de Toulouse, CNRS, IRD, UPS, Toulouse, France

[2] Institut de Physique du Globe de Paris, UMR CNRS 7154, Paris, France

[3] Observatoire Volcanologique du Piton de la Fournaise, La Plaine des Cafres, Réunion, France

Corresponding author : Valérie Chavagnac (valerie.chavagnac@get.omp.eu)

**Contents of this file:**

- Figure S1
- Table S1

## Introduction

This supporting information provide geochemical and Sr isotopic composition of hydrothermal fluids collected at LSHF.

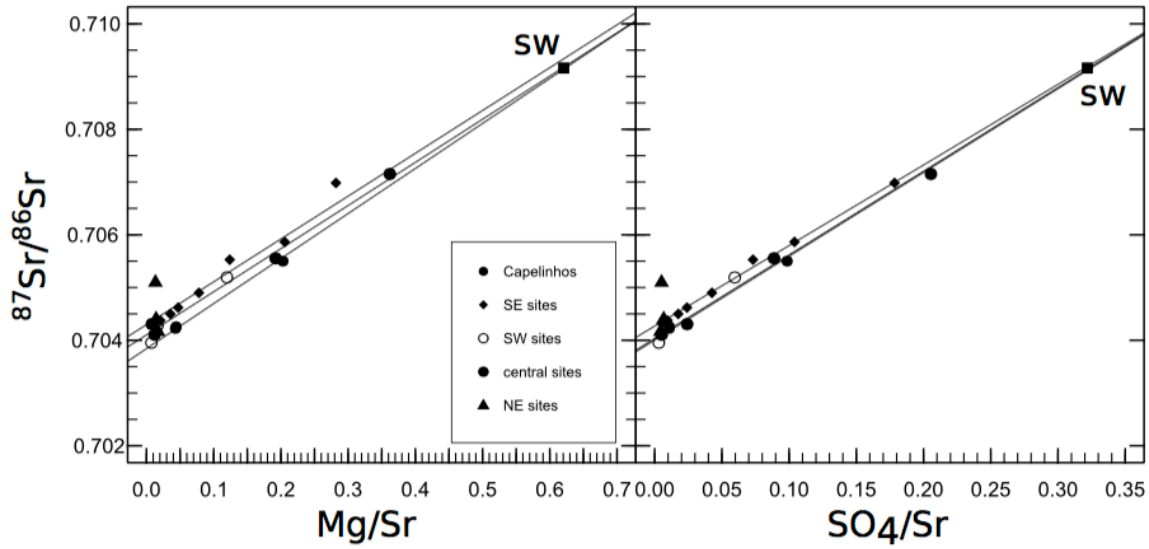


811

812 **Figure S1.** Diagram of $^{87}Sr/^{86}Sr$ as a function of Mg/Sr in (a) and $SO_4$/Sr in (b). SW stands for
813 seawater. a) shows the usual way of determining the Sr isotope signature of end-member fluids
814 based on the Mg/Sr ratio. b) is an alternative method based on sulfate concentration. Sulfate
815 contents of fluids will be dependent on seawater entrainment during sampling, as $SO_4$ is
816 enriched in seawater compared to pure hydrothermal fluid. Sulfate will also be dependent on
817 anhydrite. Dissolution of anhydrite may contribute to Ca, $SO_4$ and Sr concentrations measured
818 in the fluid and may modify its Sr isotope signature. Assuming Sr isotope signatures of seawater
819 and hydrothermal fluid, dissolution of anhydrite dissolution bias can be corrected as shown in
820 Fig S1b. Consequently, endmember determined for South-West sites are better determined by
821 $SO_4$/Sr least square regression. When no suspicion of anhydrite dissolution, Mg/Sr should be
822 preferred instead of $SO_4$/Sr, i.e. for slightly negative end-member $SO_4$ value (e.g. Capelinhos).
823 All the data are reported in Table S1.

824

**Table S1.** Geochemical compositions and Sr isotope signatures of hydrothermal fluids collected during the MoMARSAT'13 cruise. $^{87}Sr/^{86}Sr$ ratios of hydrothermal end-members are calculated by linear extrapolation to zero Mg/Sr or $SO_4$/Sr of the least-square regression method ($r^2$ are provided). All geochemical measurements made aboard the cruise are available in the cruise report at the following doi: http://dx.doi.org/10.17600/13030040.

| site | groupe | sample | Cl mM | Mg mM | SO4 mM | Sr µM | Mg/Sr | SO4/Sr | 87Sr/86Sr | r2 |
|---|---|---|---|---|---|---|---|---|---|---|
| Capelinhos | cap | M13FLU028 | 322.7 | 8.69 | 4.22 | 42.78 | 0.203 | 0.099 | 0.705501 | |
| Capelinhos | cap | M13FLU029 | 275 | 1.68 | 0.42 | 38.98 | 0.043 | 0.011 | 0.704226 | |
| Capelinhos | cap | M13FLU031 | 265.4 | 1.63 | 0.40 | 36.86 | 0.044 | 0.011 | 0.704256 | |
| | | end-member | | | | | 0 | | 0.70384 | 0.999 |
| | | end-member | | | | | | 0 | 0.704034 | 0.999 |
| Aisics | SE | M13FLU002 | 466.1 | 16.77 | 8.48 | 81.55 | 0.206 | 0.104 | 0.705865 | |
| Aisics | SE | M13FLU003 | 435 | 2.86 | 1.41 | 80.42 | 0.036 | 0.018 | 0.704499 | |
| Aisics | SE | M13FLU042 | 429.2 | 1.14 | 0.55 | 82.34 | 0.014 | 0.007 | 0.704386 | |
| Aisics | SE | M13FLU043 | 442.3 | 6.28 | 3.43 | 80.44 | 0.078 | 0.043 | 0.7049 | |
| Montségur | SE | M13FLU010 | 434.1 | 3.86 | 1.97 | 81.92 | 0.047 | 0.024 | 0.70462 | |
| Montségur | SE | M13FLU011 | 431.7 | 1.63 | 0.76 | 79.51 | 0.02 | 0.01 | 0.704376 | |
| Tour Eiffel | SE | M13FLU044 | 424.5 | 0.89 | 0.42 | 80.61 | 0.011 | 0.005 | 0.704324 | |
| Tour Eiffel | SE | M13FLU045 | 487.1 | 23.74 | 15.03 | 84.21 | 0.282 | 0.178 | 0.706983 | |
| Tour Eiffel | SE | M13FLU047 | 451.2 | 10.27 | 6.07 | 82.92 | 0.124 | 0.073 | 0.705528 | |
| | | end-member | | | | | 0 | | 0.70430 | 0.987 |
| | | end-member | | | | | | 0 | 0.704267 | 0.998 |
| Cyprès | Central | M13FLU039 | 530.7 | 1.93 | 0.48 | 111.73 | 0.017 | 0.004 | 0.704174 | |
| Isabel | Central | M13FLU008 | 497.6 | 1.55 | 0.73 | 108.61 | 0.014 | 0.007 | 0.704413 | |
| White Castle | Central | M13FLU015 | 483.4 | 1.47 | 0.57 | 110.25 | 0.013 | 0.005 | 0.705108 | |
| | | end-member | | | | | 0 | | 0.704453 | 0,969 |
| | | end-member | | | | | | 0 | 0.704487 | 0.971 |
| Crystal | SW | M13FLU022 | 563.0 | 19.16 | 8.85 | 99.66 | 0.192 | 0.089 | 0.705554 | |
| Crystal | SW | M13FLU023 | 572.6 | 1.61 | 4.93 | 203.94 | 0.008 | 0.024 | 0.704307 | |
| Sapins | SW | M13FLU049 | 576.6 | 33.87 | 19.22 | 93.54 | 0.362 | 0.205 | 0.707153 | |
| South Crystal | SW | M13FLU017 | 573.9 | 1.49 | 0.64 | 123.70 | 0.012 | 0.005 | 0.704104 | |
| | | end-member | | | | | 0 | | 0.704102 | 0,997 |
| | | end-member | | | | | | 0 | 0.704004 | 0,998 |
| Sintra | NE | M13FLU027 | 550.1 | 12.99 | 6.46 | 108.5 | 0.124 | 0.06 | 0.705191 | |
| Y3 | NE | M13FLU032 | 601.2 | 1.06 | 0.45 | 144.61 | 0.007 | 0.003 | 0.703953 | |
| Y3 | NE | M13FLU035 | 578.4 | 2.29 | 1.15 | 141.84 | 0.016 | 0.008 | 0.704275 | |
| | | end-member | | | | | 0 | | 0.704071 | 0,997 |
| | | end-member | | | | | | 0 | 0.70909 | 0,996 |
| | | seawater (SW) | | 54 | 28 | 87 | 0.621 | 0.322 | 0.709162 | |